Contents lists available at ScienceDirect

MethodsX

ELSEVIER

Method Article

Simulation of kinematic Kikuchi diffraction patterns from atomistic structures

Adam D. Herron[a], Shawn P. Coleman[c], Khanh Q. Dang[b], Douglas E. Spearot[b], Eric R. Homer[a],*

[a] Department of Mechanical Engineering, Brigham Young University, Provo, UT 84602, USA
[b] Department of Mechanical and Aerospace Engineering, University of Florida, Gainesville, FL 32611, USA
[c] U.S. Army Research Laboratory, Weapons and Materials Research Directorate, Aberdeen Proving Ground, MD 21005, USA

A B S T R A C T

One of the limitations of atomistic simulations is that many of the computational tools used to extract structural information from atomic trajectories provide metrics that are not directly compatible with experiments for validation. In this work, to bridge between simulation and experiment, a method is presented to produce simulated Kikuchi diffraction patterns using data from atomistic simulations, without requiring *a priori* specification of the crystal structure or defect periodicity. The Kikuchi pattern simulation is based on the kinematic theory of diffraction, with Kikuchi line intensities computed via a discrete structure factor calculation. Reciprocal lattice points are mapped to Kikuchi lines using a geometric projection of the reciprocal space data. This method is validated using single crystal atomistic models, and the novelty of this approach is emphasized by simulating kinematic Kikuchi diffraction patterns from an atomistic model containing a nanoscale dislocation loop. Deviations in kinematic Kikuchi line intensities are explained considering the displacement field of the dislocation loop, as is done in diffraction contrast theory.

---

* Corresponding author.
  E-mail address: eric.homer@byu.edu (E.R. Homer).

Specifications Table

Subject area	Materials Science
Method name	Simulated Kinematic Kikuchi Diffraction from Atomistic Simulation
Original Method	S.P. Coleman, D.E. Spearot, L. Capolungo, Virtual diraction analysis of Ni[010] symmetric tilt grain boundaries, Modeling and Simulation in Materials Science and Engineering.21 (2013) 055020. doi:10.1088/0965-0393/21/5/055020

Method details

This work demonstrates a method to generate simulated Kikuchi diffraction patterns directly from atomistic simulation results using the kinematic theory of diffraction. The method aims to provide a tool that can link experimental and modeling results, which can be difficult to compare. This approach may enable (1) improved crystal structure matching methods beyond existing diffraction pattern databases and (2) exploration of the role of defects on diffraction patterns without requiring simplifying assumptions regarding their spatial distribution.

Review of Coleman et al. diffraction calculations

The method is derived from the virtual diffraction algorithm developed by Coleman et al. [1,2], which computes diffraction intensities across a three-dimensional mesh of reciprocal lattice points (RELP), each described by a wave vector $\mathbf{K}$. The wave vector $\mathbf{K}$ represents the difference between the incident and diffracted wave vectors for radiation passing through a sample [3]. Diffraction intensities are strong for those RELP where the Bragg condition is satisfied,

$$|\mathbf{K}| = \frac{1}{d_{hkl}} = \frac{2\sin(\theta_B)}{\lambda} \tag{1}$$

where θ_B is the Bragg angle for the (hkl) plane of atoms, with inter-planar spacing, d_{hkl}, and wavelength of radiation, λ. When the Bragg condition is met, $\mathbf{K}$ has direction $\mathbf{g}_{hkl}$, which is normal to the plane of diffracting atoms with Miller indices (hkl). For electron diffraction, the magnitude of the diffraction intensity for any $\mathbf{K}$ is given by

$$I(\mathbf{K}) = \frac{F(\mathbf{K}) \cdot F(\mathbf{K})^*}{N} \tag{2}$$

where N is the number of atoms in the simulation. $F(\mathbf{K})$ is the atomic structure factor, given by

$$F(\mathbf{K}) = \sum_{j=1}^{N} f_j(\theta) * \exp(2\pi i\mathbf{K}\cdot\mathbf{R}_j) \tag{3}$$

where j is summed over the N atoms in the simulation cell and $\mathbf{R}_j$ gives the real space position of the jth atom in the structure. The atomic scattering factor f_j is a function that accounts for differences in scattering from different atomic species as well as losses in intensity due to Compton scattering [4]. The atomic scattering factor is unique for the species of each atom, the type of radiation simulated, and the scattering angle θ. Thus, the contribution to the diffraction intensity from all atoms in a simulation cell is calculated at each RELP. More detail on the atomic scattering factor is available in Coleman et al. [1,2] and fundamental microscopy texts [3,4]. The method can be used to calculate selected area electron diffraction (SAED) patterns as well X-ray diffraction (XRD) patterns and has been incorporated as an algorithm in the LAMMPS molecular dynamics simulation package [5].

Kikuchi diffraction

Kikuchi diffraction is observed in the transmission electron microscope (TEM) when viewing crystalline samples with thickness larger than typical for SAED pattern imaging, but thin enough that electron transparency is maintained. The larger sample thickness allows multiple diffraction events (which are nearly entirely elastic) during transmission [3]. These additional diffraction events scatter the electrons in all directions, similar to having incident beams from all angles surrounding the sample region. The Bragg condition for a single diffracting plane (*hkl*) is satisfied only for a subset of incident beam orientations whose Ewald spheres intersect with the high intensity reflection associated with the diffracting plane. In three-dimensions, this subset of incident orientations satisfying the Bragg condition for a single diffracting plane generates a Kossel cone [3], as shown in Fig. 1. While in theory, one could measure the entire cone with a spherical detector; in practice, two-dimensional detectors are used to image a portion of the Kossel cone as it intersects a view screen resulting in a Kikuchi line for each diffracting plane. Commonly, pairs of diffracting planes (*hkl* and $\overline{hkl}$) satisfy the diffraction conditions simultaneously resulting in two diverging Kossel cones in three-dimensions and Kikuchi bands in two-dimensions, as shown in Fig. 1.

Simulated kinematic Kikuchi patterns can be generated using the electron diffraction intensities computed at each RELP in three-dimensional reciprocal space [1]. Using the kinematic approach, the intensity of each Kikuchi line is equal to the computed intensity of the RELP from which it was mapped. The Kikuchi band appears on the detector screen where it intersects the Kossel cone that is associated with the RELP [3].

In practice, a way to find these intersections is to use a construct similar to the Ewald Sphere [6]. A sphere of radius λ^{-1} is drawn, centered at the origin of reciprocal space, as illustrated in Fig. 2. Henceforth, this sphere is referred to as the Kikuchi sphere. A second sphere of radius λ^{-1}, centered on the RELP of interest, is constructed and the small circle created at the intersection of these two spheres represents the Kikuchi line that would be obtained by a spherical detector. Similarly, the Kikuchi line may also be located by finding the intersection of the Kikuchi sphere and a plane perpendicular to and bisecting the wave vector **K**. Both of these methods describe the same, infinitely thin, small circle on the surface of the Kikuchi sphere, as illustrated in Fig. 2. This process has some similarities with the construction of dispersion surfaces, which are a pictorial representation of the relationship between the wave vector **K** and the electron energy [3]. It appears similar because the dispersion surfaces are created by considering two Bragg beams represented as spheres, separated by the wave vector, and their plane of intersection does correspond to the trace of the diffracting plane. However, the dispersion surfaces go far beyond this simple construction allowing one to visually understand how
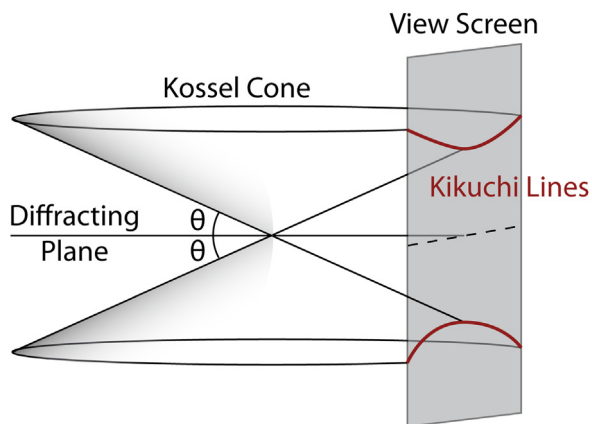
Fig. 1. Kossel cone construction, showing Kikuchi lines from a diffracting plane at the intersection of the Kossel cone and the view screen. Each cone is inclined by the associated Bragg angle θ.
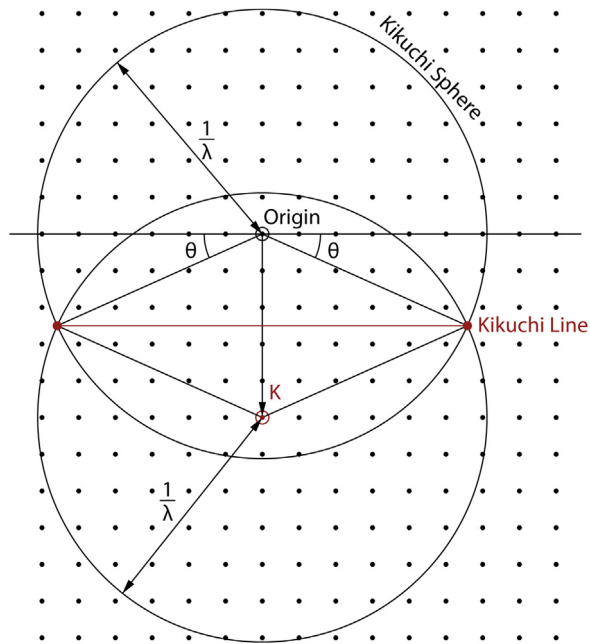
Fig. 2. Schematic showing the construction of a Kikuchi line corresponding to a single RELP in a mesh of reciprocal lattice points. The Kikuchi line is located at the Bragg angle described by the magnitude of **K** and the wavelength of the electron beam according to Bragg's Law (Eq. (1)). The Kikuchi line intersects the Kikuchi sphere at a plane perpendicular to and bisecting the wave vector **K**. The Kikuchi line is also a small circle created by the intersection of the Kikuchi sphere and a sphere centered on the RELP **K**.

electrons in a periodic potential (crystal) lead to band diagrams and band gaps as they relate to the wave vector. At a very basic level, the present approach has similarities with dispersion surfaces, but the motivation behind the two approaches is very different.

Note, the Kossel cone can be observed in this construction by combining the small circle formed on the Kikuchi sphere with the origin of the Kikuchi sphere, which acts as the cone vertex. This cone represents one of the two Kossel cones in Fig. 1, where the second would be formed from the RELP at −**K**. Each RELP sampled in the analysis of the atomistic simulation data mathematically defines one infinitely thin band mapped to the surface of the Kikuchi sphere. When all the RELP are considered, one can generate a kinematic Kikuchi diffraction pattern.

Pixel mapping for visualization

Mapping a series of geometrically defined, infinitely thin circles onto a detector, modeled as a discrete pixel array, can be solved in numerous ways. For example, the entire Kikuchi sphere can be visualized by generating a pixel array in the shape of a sphere, as demonstrated in Fig. 3 for diffraction obtained from an atomistic model of a perfect face-centered cubic (FCC) Ni single crystal. Likewise, a two-dimensional detector can be simulated by generating a planar pixel array and mapping RELP intensities onto those pixels using a gnomonic projection method. An ideal method for mapping the RELP onto the surface of the Kikuchi sphere would do so in a way that represents the data contained in the intensity values of the RELP accurately and without loss. There are a number of ways to approximate this ideal mapping, and one such method is presented here.

To map Kikuchi lines onto a two-dimensional detector using a gnomonic projection, a planar pixel array, representing the detector is first defined in real space at a distance D from the origin, as shown in Fig. 4. The location of each pixel may be defined by a vector **P**, which points from the origin to the
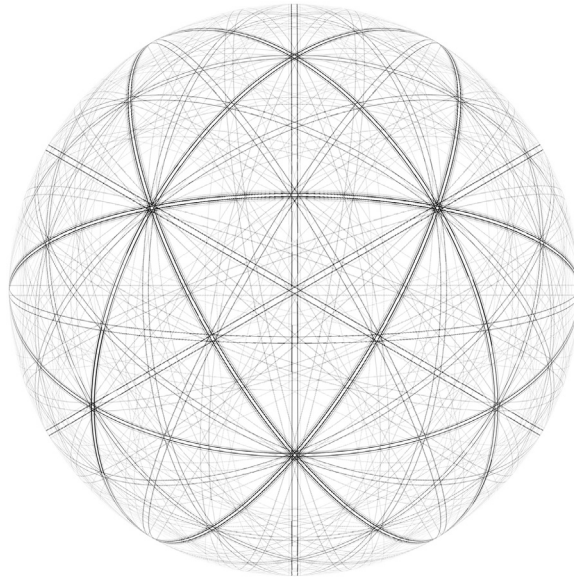
Fig. 3. Spherical projection of Kikuchi lines for a perfect FCC nickel crystal.
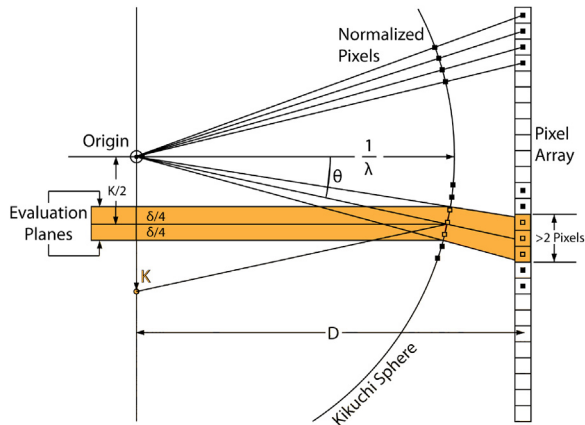
Fig. 4. Schematic illustrating the gnomonic projection of a Kikuchi lines onto a flat pixel array. RELP are mapped onto the finite pixel array by evaluating the Bragg condition for each pixel with a tolerance using a pair of parallel planes according to Eq. (5).

location of the pixel on the detector. Each RELP should map to this pixel array as a line with a finite thickness in order to avoid signal loss. Parallel Kikuchi lines mapped from RELP which represent parallel planes should also not overlap, as this will cause artificially high intensity at regions of overlap. To accommodate these requirements, the resolution of the pixel array must be sufficiently fine to capture the signal contained in the RELP intensities without aliasing. In the present work, a finite thickness of at least 2 pixel lengths is used to represent each Kikuchi line. The minimum resolution to accommodate these requirements is given in units inverse to that of the screen offset distance D and is

a function of δ, the distance between RELP,

$$\text{Resolution} \geq \frac{4}{D\delta\lambda}. \tag{4}$$

Each pixel **P**, when scaled by $\frac{1}{\lambda |\mathbf{P}|}$, lies on the surface of the Kikuchi sphere and receives intensity contributions from each RELP **K** for which it meets the Bragg condition. Mathematically, this condition is met when the vector component of **P** which lies in the direction of **K** is equal to $\frac{|\mathbf{K}|}{2}$. To map each RELP to a Kikuchi line at least 2 pixels wide and ensure that parallel Kikuchi lines do not overlap, the Bragg condition is evaluated with a tolerance of $\pm\frac{\delta}{4}$, one half of the reciprocal space distance between adjacent RELP Kikuchi lines. This evaluation can be visualized as selecting pixels with normalized position that lie between two parallel planes, as depicted in Fig. 4, and can be represented mathematically by the following inequality,

$$\frac{|\mathbf{K}|}{2} - \frac{\delta}{4} < \frac{\mathbf{K}\cdot\mathbf{P}}{|\mathbf{K}|\lambda|\mathbf{P}|} < \frac{|\mathbf{K}|}{2} + \frac{\delta}{4}. \tag{5}$$

Mapping m RELP onto an array containing n pixels requires $(n * m)$ evaluations of this inequality and can become quite computationally expensive. Intensity thresholding is an excellent way to reduce the number of RELP which are evaluated and thereby dramatically decrease the computational time required to generate a Kikuchi pattern without losing high intensity Kikuchi lines. Computational cost can also be reduced by increasing the screen distance D. This reduces the solid angle defining the portion of the Kikuchi Sphere which appears on the two-dimensional image, effectively "zooming in" on a portion of the sphere, thereby reducing the required pixel resolution.

For many reasons, it may be desirable to maintain a constant screen resolution between computations. It may also be desirable to reduce the resolution of a Kikuchi pattern for preliminary analyses where orientation information and speed are more important than relative line intensities. In such case, the resolution can be specified and Eq. (4) can be solved for a requisite effective δ, yielding,

$$\delta_{eff} = \frac{4}{\lambda\, D\, \text{Resolution}}. \tag{6}$$

If this δ_{eff} is greater than the δ which represents the distance between RELP, it can be substituted into Eq. (5), effectively setting the bandwidth of each Kikuchi line to two pixels length on the view screen. This ensures that each RELP contributes to the Kikuchi pattern and that no RELP are missed by falling into the gaps between pixels. It is noted, however, that using $\delta_{eff} > \delta$ introduces aliasing into the signal, artificially increasing band intensities where parallel Kikuchi lines will overlap. In the case that δ_{eff} is smaller than the original δ, the original δ should be used and each RELP will contribute to a band more than two pixels wide without aliasing.

Since the images are a map of intensity, one can use any color map to represent the data. In this work, data is presented in grayscale or inverted grayscale. In the generation of experimental Kikuchi patterns it is possible to get inverted patterns or band profiles depending upon the angle of incidence and the placement of the detector [7]. One could use known conditions to select an appropriate color map, but because the intensity units in this work are arbitrary, we select grayscale or inverted grayscale maps for optimal comparison and viewing.

Additional information

The additional information provided with this method is divided into four sections. The first section provides a comparison of Kikuchi diffraction patterns created by this method with experimentally obtained Kikuchi diffraction patterns for a variety of crystal structures. The second section applies the technique to a single dislocation loop and analyzes the results in the context of what is known about the dislocation loop and what can be extracted from the simulated Kikuchi pattern. The third section provides context for the technique in relation to other work focused on simulating diffraction patterns, along with a discussion of the limitations of the method. The final section provides concluding remarks on the method.

Simulated and experimental Kikuchi patterns of single crystals

Several different crystal structures are considered to provide basic verification of the technique to simulate kinematic Kikuchi diffraction patterns from an ensemble of atoms arranged as a single crystal, without manually specifying the crystal structure periodicity in the diffraction algorithm. Verification is accomplished through visual comparison of the simulated Kikuchi patterns with experimentally obtained Kikuchi patterns from the literature. Verification is also accomplished by ensuring that the Kikuchi bands are at correct positions and angles from one another. The visual comparison with the experimental Kikuchi patterns is not definitive validation, but the examination of the band positions and angles ensures self-consistency.

Three different perfect crystal structures are examined using interatomic potentials for the following materials: face-centered cubic (FCC) Ni using the Foiles-Hoyt embedded atom method (EAM) potential [8], body-centered cubic (BCC) Fe using the Mendelev EAM potential [9], and hexagonal close packed (HCP) Zr using another Mendelev EAM potential [10]. LAMMPS [5] is used to create minimum energy crystal structures with $10 \times 10 \times 10$ unit cells for each material. The approach by Coleman et al. is used to determine diffraction intensities at each RELP with $\lambda = 0.0251$ Å, a wavelength corresponding to an excitation voltage of a 200 keV electron microscope. For these simulated images, the reciprocal lattice was sampled with a resolution of one-half the lattice parameter for each material, resulting in cubic reciprocal space meshes with spacing 0.056818 Å^{-1}, 0.070045 Å^{-1}, and 0.061900 Å^{-1} for Ni, Fe, and Zr respectively. The methodology described in the previous sections is used to generate the simulated kinematic Kikuchi diffraction intensities and patterns. These images are generated using a screen width of 6 in, height of 4 in, placed at a distance of 3 in from the origin, and pixel resolution of 512 dpi.

Figs. 5–7 present patterns and maps for FCC, BCC, and HCP structures, respectively. The simulated kinematic Kikuchi diffraction patterns are compared to standard Kikuchi maps and experimental Kikuchi diffraction patterns collected from the literature [3,11]. The simulated patterns have been truncated to focus on the common regions in the maps and experimental patterns.

a.　　　　　　　　　　b.　　　　　　　　　　c.
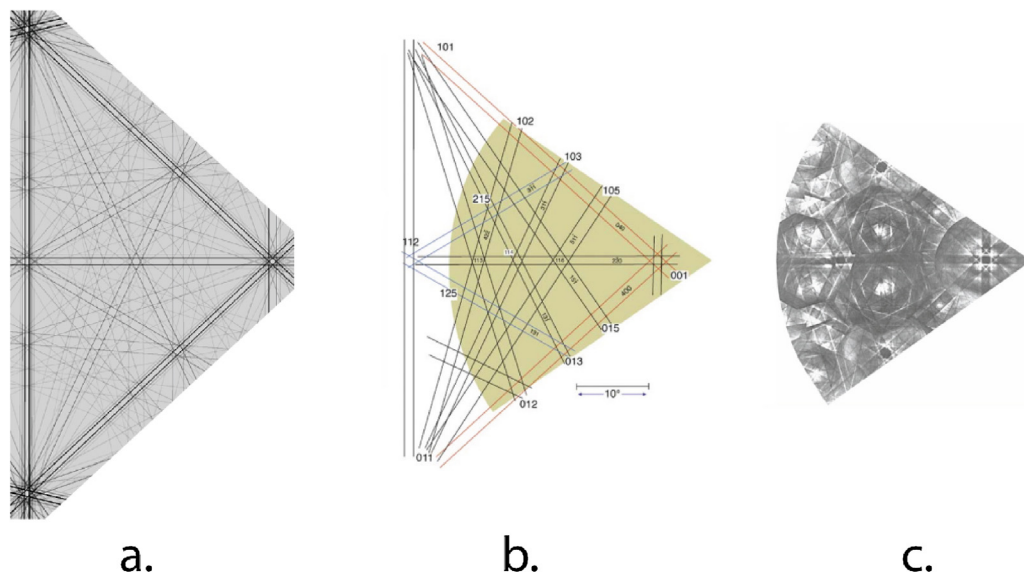
Fig. 5. Comparison of the (a) simulated Kikuchi pattern generated from a perfect FCC Ni crystal model, (b) standard textbook FCC Kikuchi pattern and (c) experimentally collected and stitched TEM diffraction pattern. Parts (b) and (c) are reproduced with permission from [3].
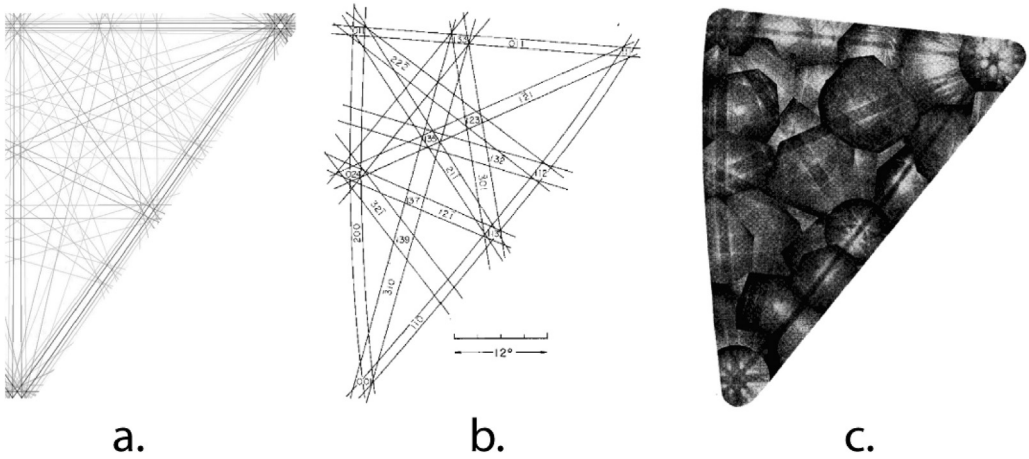
Fig. 6. Comparison of the (a) simulated Kikuchi pattern generated from a perfect BCC Fe crystal model, (b) standard textbook BCC Kikuchi pattern, and (c) experimentally collected and stitched TEM diffraction pattern. Parts (b) and (c) are reproduced with permission from [11].

In each case, the simulated kinematic Kikuchi patterns show all low-index bands in the expected positions and with the expected bandwidths. For example, in the case of the simulated Ni patterns, the {100} plane Kikuchi lines are separated by a band width of approximately 22 pixels, corresponding to a Bragg angle of 0.409 degrees and thus an interplanar spacing of 1.752 Å. This is a relative error of 0.430% from the experimentally observed value of 1.760 Å for Ni {100} planes. This accuracy can be further improved by changing the pixel resolution or screen distance parameters for the simulation, at the expense of computation time or field of view, respectively.

In the case of the FCC pattern in Fig. 5, the Kikuchi map (Fig. 5b) denotes the overlap of the experimental pattern (Fig. 5c) with the map in the light brown shaded region, so only part of the experimental pattern overlaps the simulated pattern. In the case of the BCC pattern in Fig. 6, the Kikuchi map (Fig. 6b) and experimental pattern (Fig. 6c) have bands on the boundary that are curved. In contrast, the same bands in the simulated pattern (Fig. 6a) are perfectly straight. This discrepancy is attributed to the gnomonic projection of the bands on the surface of the Kikuchi sphere onto a flat pixel array. For the HCP comparison in Fig. 7, different simulation images are used for the map and experimental comparison in an effort to identify similarities. The experimental pattern has curved bands at the boundary while the Kikuchi map and simulated patterns do not. In all cases, the major low-index bands can be clearly identified in the simulated Kikuchi patterns and many higher-index bands, not identified in the standard maps can be seen in the simulated and experimental patterns.

The intensity of the simulated bands is not generally in harmony with the intensity of the experimental diffraction patterns, though methods exist to correct these differences [12]. The discrepancies in intensity are attributed to the kinematic nature of the method and the discrete pixel mapping, which does not account for the complex nature of the diffracting signal and the constructive and destructive interference that can occur [13]. This simplification removes all phase information from the signal and simply sums the intensity contributions of each RELP at each detector pixel. Although somewhat non-physical in this respect, this has both benefits and weaknesses. For example, in the simulated kinematic Kikuchi patterns, the identification of specific bands, and any changes to band position will be more easily identified (compare Fig. 6a and c). As bands are generated from atomistic data, this may enable unambiguous connections between Kikuchi patterns and atomic level structure. However, the kinematic nature could complicate efforts to interpret an experimental Kikuchi pattern using only simulated Kikuchi patterns of relevant atomistic structures. Nevertheless, this method is able to produce patterns without *a priori* specification of the crystal structure periodicity, and thus could be advantageous in identifying discrete features of the crystal structure.
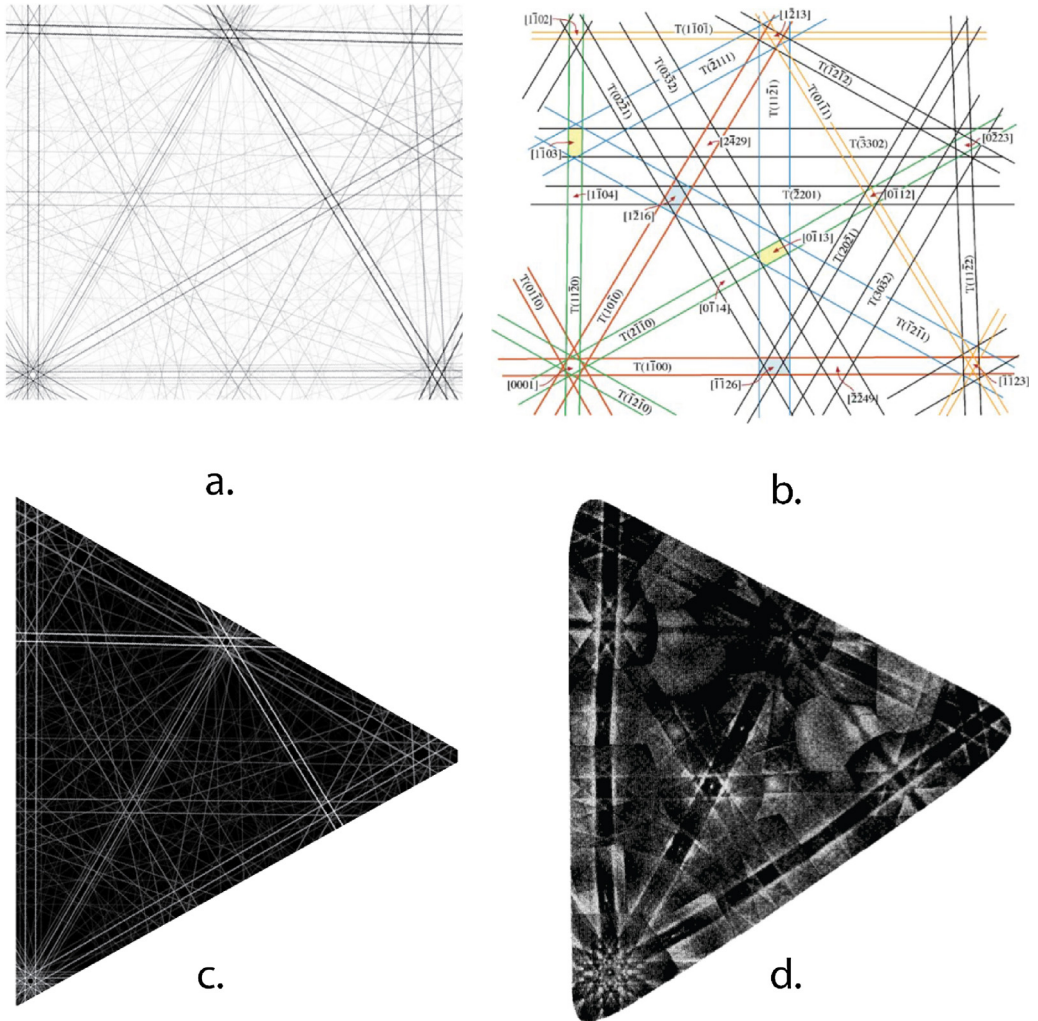
Fig. 7. Comparison of the (a) simulated Kikuchi pattern generated from a perfect HCP Zr crystal model with the (b) standard textbook HCP Kikuchi pattern, as well as (c) an inverted simulated diffraction pattern centered on a different zone for comparison with (d) an experimentally collected and stitched TEM diffraction pattern. Parts (b) and (d) are reproduced with permission from [3,11], respectively.

Diffraction from a dislocation shear loop

To illustrate that the current method can produce kinematic Kikuchi diffraction patterns using atomistic simulation data which includes defects, the method is applied to the analysis of an atomistic model containing a nanoscale dislocation loop, as shown in Fig. 8. A dislocation loop with radius 8.10 nm is constructed on the $(111)[\bar{1}01]$ slip system using a modification of the approach presented by Bitzek et al. [14]. Briefly, this method constructs dislocation loops via superposition of displacement fields from eight triangular dislocations, which were derived originally by Barnett [15]. The displacement field solution of Barnett does not describe the atom displacements close to the dislocation core; thus, energy minimization (via the FIRE algorithm [16]) is performed after the insertion of the octagonal dislocation geometry. Energy minimization is performed under an applied
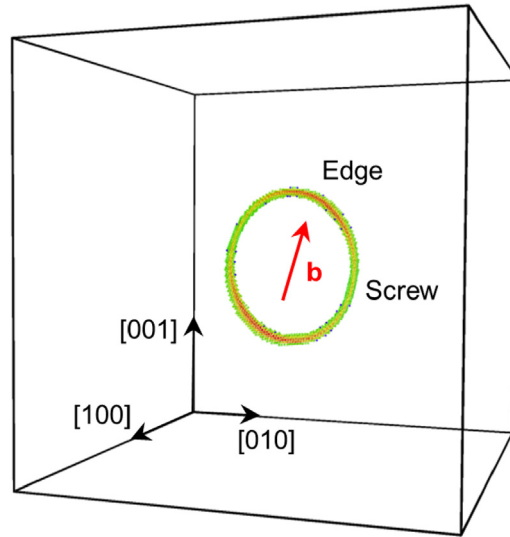
Fig. 8. Dislocation loop geometry with 8.10 nm radius and Burgers vector $[\bar{1}01]$ constructed using an energy minimization procedure. Atoms with centrosymmetry parameter less than $2.0\,\text{Å}^2$ are removed so that the dislocation core structure is visible.

shear stress of 0.504 GPa in the Burger's vector direction to prevent the loop from collapsing. This shear stress is in decent agreement with the theoretical prediction by Scattergood and Bacon [17] for this size dislocation loop.

A cubic simulation cell with length 28.35 nm on each side (1.372 million atoms) is employed for both the dislocation loop model and a single crystal model without the dislocation loop. Periodic boundary conditions are applied in all directions so that free surfaces are eliminated. For both dislocation loop and single crystal models, electron diffraction ($\lambda = 0.0251$ Å) intensities are computed across a cubic reciprocal space mesh with spacing $0.007166\,\text{Å}^{-1}$, resulting in approximately 58.589 million RELP sampled. This reciprocal space mesh is sufficiently fine to capture all necessary kinematic details of the Kikuchi diffraction pattern. The scalar value of the intensity at each RELP is used to determine the intensity of each Kikuchi band as explained in the method details (Sections "Kikuchi diffraction" and "Pixel mapping for visualization").

Fig. 9 shows simulated kinematic Kikuchi diffraction patterns viewed on the [001] and [1$\bar{1}$0] zones for the 8.10 nm dislocation loop model and a single crystal model under an identical state of stress without the dislocation loop. Images are generated using a screen width of 4 in, screen height of 4 in, placed at a distance of 4 in from the origin, and pixel resolution of 256 dpi. The raw diffraction intensities illustrate that the presence of the 8.1 nm radius dislocation loop generally reduces the intensities of the individual kinematic Kikuchi bands, especially for the higher-index bands. This is because the displacement field of the dislocation loop provides a gradient of displacements to the regular atom positions, which gradually changes the spacing between lattice planes. Thus, a measurable reduction in the intensities, especially for the higher–index planes, and a blurring of the Kikuchi lines is expected.

Since the kinematic Kikuchi patterns are computed using an identical number of atoms and identical number of RELP, one can directly compare specific features of the two simulated patterns. The change in the diffraction pattern due to the presence of the dislocation loop can be visualized by subtracting the diffraction intensities at each pixel. This difference is shown in Fig. 10. In this difference figure, darker bands represent crystallographic planes that are influenced to a greater extent by the displacement field of the dislocation loop; in other words, the darker the band is in the difference image, the larger the decrease in intensity in the dislocation loop diffraction patterns in Fig. 9. There is
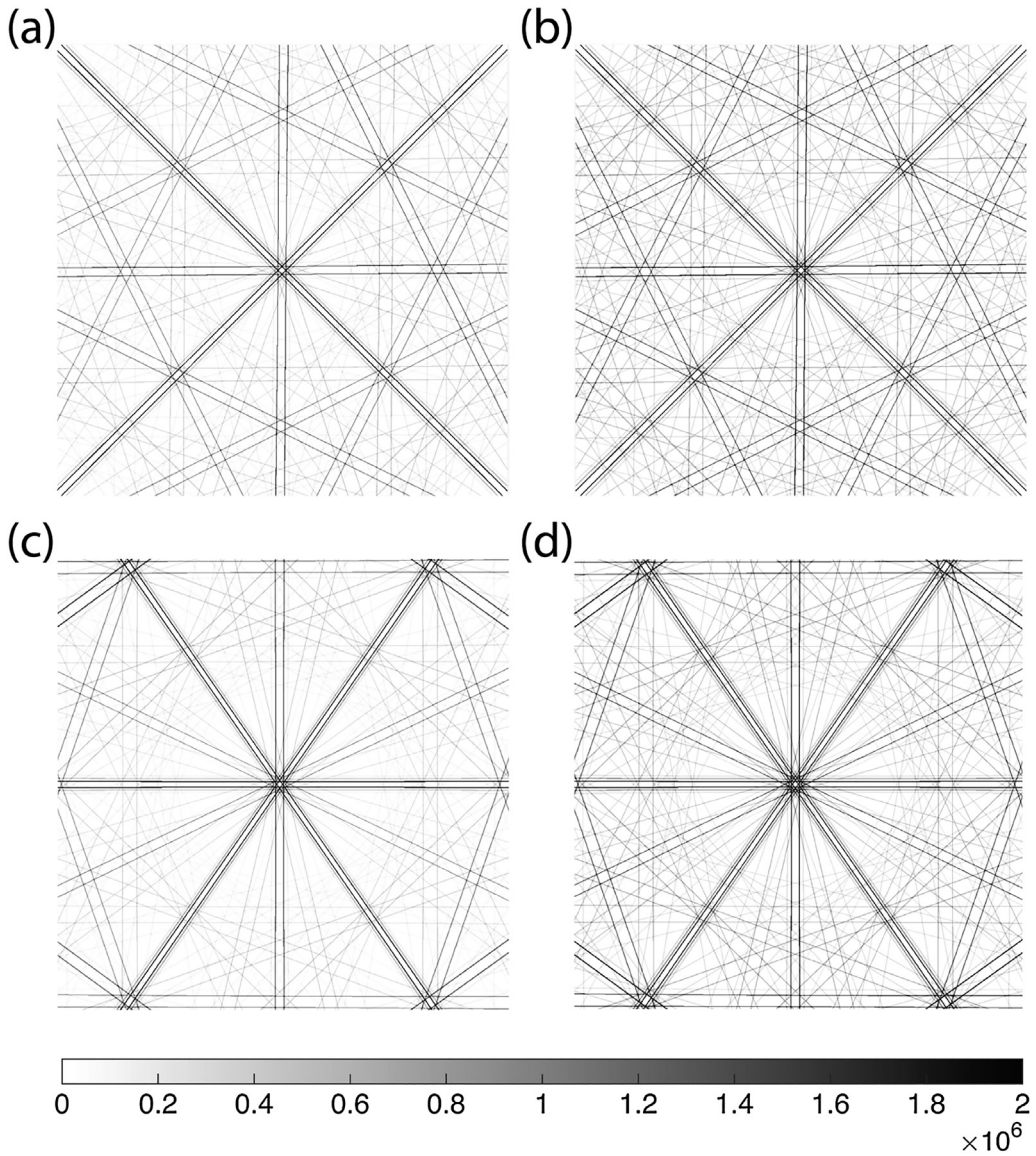
Fig. 9. Kikuchi diffraction patterns for the dislocation loop model and the single crystal model focused on the [001] zone in (a) and (b), respectively, and the [1$\bar{1}$0] zone in (c) and (d), respectively.

a clear asymmetry in the way that the intensities of the different Kikuchi bands within the same family are influenced. For example, in Fig. 10a, the (010) band is less influenced than the (100) band; while in Fig. 10b, the (111) band is less influenced than the (11$\bar{1}$) band. Table 1 lists the intensity values, in arbitrary units, for the single crystal, I^{SX}, and the dislocation loop, I^{DL}, for the {100}, {110}, and {111} families of planes. Table 1 also lists the difference in intensities, and percent change in intensities, between the two models.
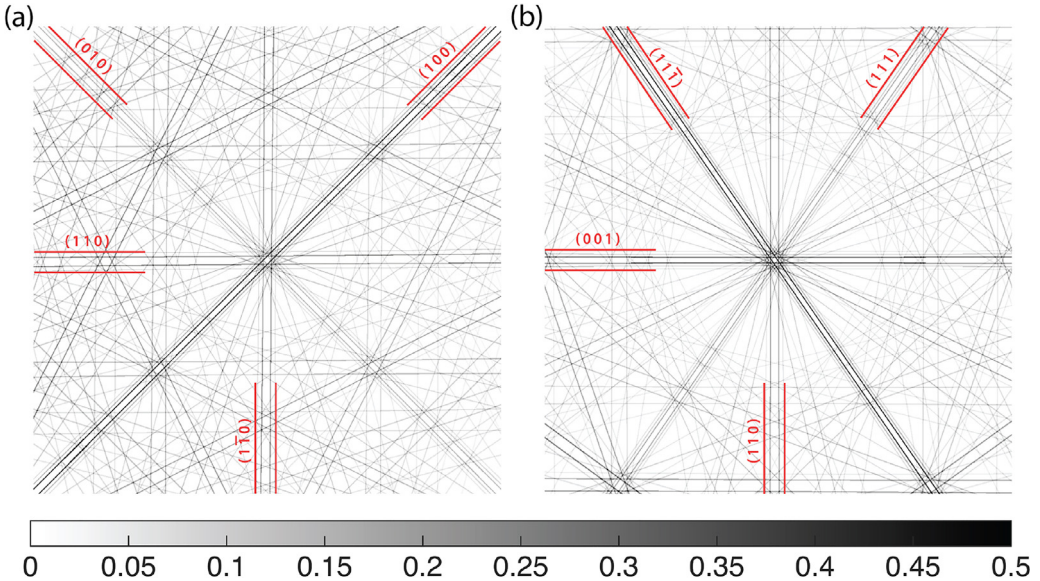
Fig. 10. Scaled difference between Kikuchi diffraction patterns from a single crystal and the dislocation loop model for the (a) [001] zone and (b) [1$\bar{1}$0] zone. Stronger intensities indicate a larger difference between the single crystal and dislocation loop Kikuchi diffraction patterns.

These observations can be related to the displacement field of this specific dislocation loop, which is a function of the Burger's vector, $\mathbf{b} = [\bar{1}01]$. Consider the screw segment of the dislocation loop where atomic displacements due to the defect are solely in the direction of the Burger's vector. Thus, crystal planes that contain the Burger's vector, such as (010) or (111) will be displaced in the direction of $\mathbf{b}$, but the spacing between these atomic planes will not change, meaning their diffraction intensity will not change (ignoring effects from the dislocation core). This observation is in agreement with the $\mathbf{g} \cdot \mathbf{b}$ contrast theory used to image screw dislocations in a TEM.

However, these planes are not completely unaffected by the dislocation shear loop. The edge segment of the dislocation loop will induce atomic displacements in a plane perpendicular to the

Table 1
Comparison of simulated Kikuchi diffraction intensity values and atomic displacements resulting from the dislocation loop for low-index planes. Units for the diffraction intensity values are arbitrary.

Family	hkl	I^{SX}	I^{DL}	$I^{SX} - I^{DL}$	$\frac{I^{SX}-I^{DL}}{I^{SX}}$ [%]	D_{hkl} [Å]	f_{hkl} [%]
100	(100)	4.10E+6	3.19E+6	9.13E+5	22%	1.31E+5	57%
	(010)	4.28E+6	4.02E+6	2.59E+5	6%	8.08E+4	35%
	(001)	4.45E+6	3.48E+6	9.74E+5	22%	1.33E+5	58%
110	(110)	1.67E+6	1.19E+6	4.80E+5	29%	1.17E+5	51%
	(101)	1.70E+6	1.52E+6	1.79E+5	11%	6.72E+4	29%
	(011)	1.74E+6	1.21E+6	5.22E+5	30%	1.23E+5	54%
	(1$\bar{1}$0)	1.67E+6	1.27E+6	4.00E+5	24%	1.03E+5	45%
	(10$\bar{1}$)	1.70E+6	1.03E+6	6.74E+5	40%	1.83E+5	80%
	(01$\bar{1}$)	1.74E+6	1.37E+6	3.65E+5	21%	9.80E+4	43%
111	(111)	6.17E+6	5.72E+6	4.52E+5	7%	9.60E+4	42%
	(11$\bar{1}$)	6.17E+6	4.88E+6	1.29E+6	21%	1.50E+5	66%
	(1$\bar{1}$1)	6.17E+6	6.10E+6	7.27E+4	1%	3.99E+4	17%
	(1$\bar{1}\bar{1}$)	6.17E+6	4.80E+6	1.37E+6	22%	1.56E+5	68%

dislocation core. Thus, the displacement field associated with the edge component of the dislocation loop will influence the spacing between (010) and (111) planes, leading to a reduction in the kinematic Kikuchi pattern intensities. Similar reasoning can be used to explain why the (10$\bar{1}$) plane is strongly affected since the Burger's vector of the dislocation loop lies perpendicular to this plane and will create a gradient of displacement perpendicular to this plane, influencing plane spacing and hence diffraction intensity. This observation is in agreement with the $\mathbf{g} \cdot \mathbf{b} \times \mathbf{u}$ contrast theory used to image dislocations with edge or mixed characters in a TEM.

To further explain the intensity difference asymmetry in terms of the displacement field of the dislocation shear loop, we examine the displacements of the atoms in the dislocation loop model relative to the atoms in the single crystal model. Here we define the cumulative displacement of the atoms between the two models in specific directions that correspond to normals, $\hat{\mathbf{g}}_{hkl}$, for the (hkl) planes. Note that here $\hat{\mathbf{g}}_{hkl}$ is a unit vector in the direction of $\mathbf{g}_{hkl}$. This is accomplished by finding the difference in atomic positions between the two models and then dotting this displacement into specific $\hat{\mathbf{g}}_{hkl}$ normals with unit length,

$$D_{hkl} = \sum_{j=1}^{N} \left| \left(\mathbf{R}_j^{DL} - \mathbf{R}_j^{SX} \right) \cdot \hat{\mathbf{g}}_{hkl} \right| \tag{7}$$

where $\mathbf{R}$ are the positions of atoms in the dislocation loop (DL) and single crystal (SX) models, as designated by the superscript. D_{hkl} describes the cumulative displacement magnitude of all atoms in a specific crystallographic direction, including those in the inverse direction. The dot product between the displacement field and the diffraction vector appears in the Howie-Whelan equations [3], which relates the change in diffraction amplitude (intensity) to a known displacement field. To extend this concept, we define the quantity,

$$f_{hkl} = \frac{D_{hkl}}{\sum_{j=1}^{N} \| \mathbf{R}_j^{DL} - \mathbf{R}_j^{SX} \|}. \tag{8}$$

In other words, f_{hkl} accounts for the fractional magnitude of the atomic displacements that point in a specific direction. The values of D_{hkl} and f_{hkl} are given for the different planes in Table 1.

From this tabulated data, it is clear that there is a general correlation between the percentage change in a plane's diffraction intensity and the fraction of atomic displacements in the same direction as the normal to the plane, as is expected from the Howie–Whelan equations. This is illustrated graphically in Fig. 11.

The presented kinematic Kikuchi diffraction method clearly captures changes in the diffraction patterns associated with an extended defect. It is important to note, however, that while this method is physically based, it uses the kinematic theory and not the dynamical theory of diffraction to provide intensities for the simulated patterns. Prior work, noted in Section "Context, limitations, and capabilities of the method" that follows, has shown that dynamical models for Kikuchi pattern simulation provide images in better agreement with experiment; however, at present there are no known methods to simulate dynamical Kikuchi patterns for extended defects. Thus, the intensity differences in Fig. 10 will likely be different in the case of dynamical diffraction, but the observation of crystallographic asymmetries in the way that a dislocation loop with known slip system influences diffraction intensities is valid and in agreement with contrast imaging theory. Thus, this observation has relevance to diffraction-based analyses of a textured metallic material, for example, where the majority of the dislocations are on a given slip system. This important first step to connect atomistic simulation and Kikuchi diffraction will motivate future work towards simulated Kikuchi patterns using dynamical theories of diffraction from multimillion atom atomistic simulation data, which remains an open challenge.

Context, limitations, and capabilities of the method

Diffraction is well established as a key experimental characterization method used to resolve and understand the structure of materials. Techniques for both X-ray and electron diffraction analysis of
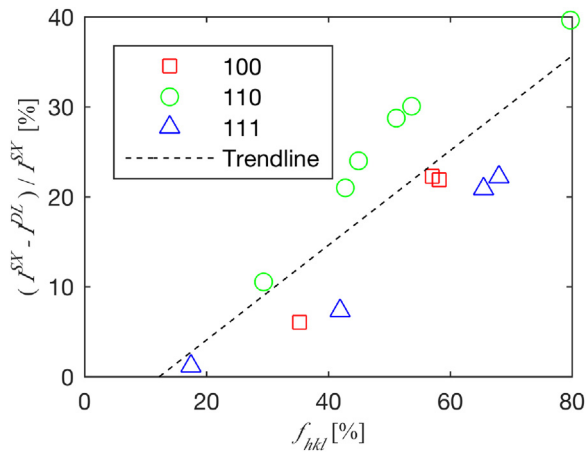
Fig. 11. Plot of change in diffraction intensity between the two atomistic models, $\left(I^{SX} - I^{DL}\right)/I^{SX}$, as a function of the fractional magnitude of displacement between the two atomistic models, f_{hkl}, for specific (hkl) planes. Note the general correlation between the two metrics, and the fact that a measurable displacement, f_{hkl}, must be accumulated before the intensity is affected.

crystalline structures are well known and well documented [3,4]. Conversely, atomistic simulation has emerged more recently as a powerful computational tool to investigate the atomic structure and behavior of materials [18]. Unfortunately, many of the tools used to analyze atomistic simulation structures are not directly compatible with experiment. For example, the centrosymmetry parameter [19] is a powerful tool to identify defects, but does not provide a metric that can be measured experimentally for validation purposes. Thus, it is necessary to develop advanced techniques to connect atomistic simulations with experiment.

Initial efforts to produce kinematic diffraction patterns from atomistic simulation data required prior specification of the crystal structure or the atomic periodicity of the defect in the sample [20–22]. These works provided important verification of the periodicity of grain boundary structures in metallic materials via experimental/computational comparisons. Removing the need to *a priori* specify the crystal or defect periodicity, several authors have developed implementations of the Debye equation to generate XRD 2θ line profiles of nanocrystalline atomistic samples [23–25]. These approaches enabled the prediction of average grain size and an analysis of microstrain from the broadening of the diffraction peaks. More recently, new models that explore three-dimensional reciprocal space using kinematic diffraction theory were developed to compute XRD line profiles and SAED patterns from multimillion atom molecular dynamics simulations [1,2,26–30]. All these methods are reminiscent of earlier direct Fourier transform methods [31], but leverage high performance parallel computing and do not require *a priori* assumption of the crystal structure or defect periodicity in the sample. They have been applied to study the structure of shocked crystalline metals [26], metal and ceramic grain boundaries, composite interfaces [1,2,29,30], and magnetic contributions to the diffraction pattern [27]. With these new computational tools, researchers can better understand how atomic-scale structure, including defect content, influences diffraction patterns in complex material systems, and can validate atomistic simulations through comparison with complementing experimentation.

Using kinematic diffraction calculations, Coleman et al. computed X-ray and electron diffraction intensities in the reciprocal space domain. XRD line profiles representing powder diffraction conditions were generated by spherically binning the three-dimensional diffraction data from the origin of reciprocal space, accounting for all possible orientations. SAED patterns were generated by taking a slice (with small numerical thickness) of the three-dimensional diffraction data representing the intersection of the Ewald sphere for a given wavelength of radiation.

Kikuchi diffraction patterns, and their related electron backscatter diffraction (EBSD) patterns, have also been simulated using kinematic and dynamical theories of diffraction [12,13,32–39].

Dynamical diffraction approaches, including Bloch waves and the scattering matrix formalism, generate simulated patterns with a high degree of fidelity, as indicated by comparison with experimental patterns [40]. However, these methods can be computationally expensive and are limited to modeling defect structures that can be represented as displacement fields. De Graef et al. have addressed the computational expense by creating a dictionary of previously computed diffraction patterns in order to make indexing simpler [41], but these are still unable to address complex, atomic-scale defects in large-scale models. In contrast, kinematic techniques generate patterns which, while less accurate than dynamical patterns, can be produced on the fly [32] and from large-scale atomistic models.

As discussed in the method details above, the method of Coleman et al. [2] is extended here to generate kinematic Kikuchi diffraction patterns directly from large atomistic structures of unknown orientation and defect content. Of course, because kinematic diffraction theory considers only a single diffraction event from a plane of atoms, there are known limitations to the interpretation of computed kinematic intensities [13]; where applicable, these limitations have been noted throughout the manuscript, but a comprehensive list is given here. First, all the bands in the patterns shown here are constructive; no destructive interference is possible as we sum the intensity of different bands at each pixel. Second, the computed bands have square profiles equal to the intensity of the corresponding RELP. The computed bands do not have profiles like those seen in experimentally obtained Kikuchi patterns or the solid bands obtained in electron backscatter diffraction (EBSD) patterns from thicker samples [7]. Third, there are no differences in intensity between two bands that would otherwise exhibit Excess and Deficient lines [3]. Fourth, there are no dynamic effects so the present method cannot capture complex interactions that allow simulated patterns to mimic experimentally obtained patterns [12]. It is possible that these complex changes could be misinterpreted in a kinematic Kikuchi pattern simulated by the present technique. Fifth, the method does not capture the fact that one can obtain inverted EBSD patterns depending upon the position of the detector.

Despite these limitations, the positions of the diffraction bands from kinematic Kikuchi and EBSD patterns are not influenced by multiple diffraction events and these positions have been used for orientation identification as well as for measurement of lattice strain and distortion [42]. Dynamic pattern simulation would be more accurate than the present method, but to the authors' knowledge this is the only known method that can simulate Kikuchi patterns of extended defects within large-scale atomic models. The ability to capture features of these extended defects is demonstrated in the analysis of the dislocation loop, where the Kikuchi pattern captures changes in the structure that are verified by other means. It is hoped that that this method will serve as a useful tool until such time as a dynamical diffraction method can be developed that can examine the effects of extended defects.

Concluding remarks

The present work demonstrates a technique for producing simulated kinematic Kikuchi diffraction patterns from atomistic data, building upon prior work by Coleman et al. that enables the creation of X-ray and selected area electron diffraction patterns from atomic positions and species [1,2]. The current work uses Bragg's Law to construct Kikuchi bands from diffracting wave vectors in reciprocal space. Methods for image creation based on the data are presented. Results are validated against standard Kikuchi maps and experimentally obtained Kikuchi diffraction patterns for FCC, BCC, and HCP crystal structures. To emphasize the value of this work towards the analysis of atomistic structures containing defects, the method is extended to study the effect of a nanoscale dislocation loop on a kinematic Kikuchi diffraction pattern. Based on this work the following conclusions are obtained about the simulated kinematic Kikuchi diffraction patterns:

- The simulated patterns from single crystal atomistic samples exhibit all low-index planes included on standard Kikuchi maps. In addition, the position of planes in the simulated Kikuchi patterns for a given zone axis are in good agreement with experiments. The simulated patterns exhibit proper band width in agreement with the expected Bragg angles from the ideal unit cell of the material.
- The kinematic construction leads to patterns that resemble the Kikuchi maps more than the experimental patterns. This is a well-known limitation of the kinematic model for simulating

Kikuchi diffraction patterns [13]. Future work must bridge this divide connecting simulated dynamical Kikuchi diffraction with atom positions and species from atomistic simulation results.

- Changes in the Kikuchi patterns due to the presence of a nanoscale dislocation shear loop are observed. Generally, a decrease in the kinematic intensity of each low-index band in the Kikuchi pattern is observed. However, certain bands are influenced more strongly than others. These observations can be linked to the measured displacement field of the dislocation loop in agreement with contrast imaging theory.

The method presented here may have additional applications within the fields of atomistic and molecular dynamics simulation. It may be particularly useful for large, noisy data sets where crystal structure or orientation is unknown and difficult or impossible to determine via other means, such as Common Neighbor Analysis. Such areas could include atom probe tomography, grain boundary modeling and characterization, structure identification in biological fields, and thermodynamic studies of highly-disordered or fluctuating materials.

Acknowledgments

References

[1] S.P. Coleman, D.E. Spearot, L. Capolungo, Virtual diffraction analysis of Ni [010] symmetric tilt grain boundaries, Model. Simul. Mater. Sci. Eng. 21 (2013) 055020, doi:http://dx.doi.org/10.1088/0965-0393/21/5/055020.

[2] S.P. Coleman, M.M. Sichani, D.E. Spearot, A computational algorithm to produce virtual X-ray and electron diffraction patterns from atomistic simulations, JOM 66 (2014) 408–416, doi:http://dx.doi.org/10.1007/s11837-013-0829-3.

[3] D.B. Williams, C.B. Carter, The Transmission Electron Microscope, Springer, New York, 2009, doi:http://dx.doi.org/10.1007/978-0-387-76501-3_1.

[4] B.E. Warren, X-Ray Diffraction, 1st edition, Dover Publications, New York, 1990.

[5] S. Plimpton, Fast Parallel Algorithms for Short-Range Molecular Dynamics, J Comput Phys 117 (1995) 1–19, doi:http://dx.doi.org/10.1006/jcph.1995.1039.

[6] P.P. Ewald, Introduction to the dynamical theory of X-ray diffraction, Acta Crystallogr. Sect. A 25 (1969) 103–108, doi:http://dx.doi.org/10.1107/S0567739469000155.

[7] L. Reimer, Scanning Electron Microscopy, Springer-Verlag, Berlin, 1985.

[8] S.M. Foiles, M.I. Baskes, M.S. Daw, Embedded-atom-method functions for the FCC metals Cu, Ag, Au, Ni, Pd, Pt, and their alloys, Phys. Rev. B 33 (1986) 7983–7991, doi:http://dx.doi.org/10.1103/PhysRevB.33.7983.

[9] M.I. Mendelev, S. Han, D.J. Srolovitz, G.J. Ackland, D.Y. Sun, M. Asta, Development of new interatomic potentials appropriate for crystalline and liquid iron, Philos. Mag. 83 (2003) 3977–3994, doi:http://dx.doi.org/10.1080/14786430310001613264.

[10] M.I. Mendelev, G.J. Ackland, Development of an interatomic potential for the simulation of phase transformations in zirconium, Philos. Mag. Lett. 87 (2007) 349–359, doi:http://dx.doi.org/10.1080/09500830701191393.

[11] P.R. Okamoto, Kikuchi maps for HCP and BCC crystals, J. Appl. Phys. 38 (1967) 289, doi:http://dx.doi.org/10.1063/1.1708968.

[12] S. Zaefferer, On the formation mechanisms, spatial resolution and intensity of backscatter Kikuchi patterns, Ultramicroscopy 107 (2007) 254–266, doi:http://dx.doi.org/10.1016/j.ultramic.2006.08.007.

[13] A. Winkelmann, G. Nolze, M. Vos, F. Salvat-Pujol, W.S.M. Werner, Physics-based simulation models for EBSD: advances and challenges, IOP Conf. Ser.: Mater. Eng. 109 (2016) 012018, doi:http://dx.doi.org/10.1088/1757-899X/109/1/012018.

[14] E. Bitzek, C. Brandl, D. Weygand, P.M. Derlet, H.V. Swygenhoven, Atomistic simulation of a dislocation shear loop interacting with grain boundaries in nanocrystalline aluminium, Model. Simul. Mater. Sci. Eng. 17 (2009) 55008, doi:http://dx.doi.org/10.1088/0965-0393/17/5/055008.

[15] D.M. Barnett, The displacement field of a triangular dislocation loop, Philos. Mag. A 51 (1985) 383–387, doi:http://dx.doi.org/10.1080/01418618508237562.

[16] E. Bitzek, P. Koskinen, F. Gähler, M. Moseler, P. Gumbsch, Structural relaxation made simple, Phys. Rev. Lett. 97 (2006) 170201, doi:http://dx.doi.org/10.1103/PhysRevLett.97.170201.

[17] R.O. Scattergood, D.J. Bacon, Dislocation shear loops in anisotropic crystals, Phys. Status Solidi (a) 25 (1974) 395–404, doi:http://dx.doi.org/10.1002/pssa.2210250204.

[18] E.B. Tadmor, R.E. Miller, Modeling Materials, Continuum, Atomistic and Multiscale Techniques, Cambridge University Press, Cambridge, 2011.

[19] C.L. Kelchner, S. Plimpton, J. Hamilton, Dislocation nucleation and defect structure during surface indentation, Phys. Rev. B 58 (1998) 11085–11088, doi:http://dx.doi.org/10.1103/PhysRevB.58.11085.

[20] P. Bristowe, S. Sass, The atomic structure of a large angle [001] twist boundary in gold determined by a joint computer modelling and X-ray diffraction study, Acta Metall. 28 (1980) 575–588, doi:http://dx.doi.org/10.1016/0001-6160(80)90124-8.

[21] P. Bristowe, R. Balluffi, Effect of secondary relaxations on diffraction from high-Σ [001] twist boundaries, Surf. Sci. 144 (1984) 14–27, doi:http://dx.doi.org/10.1016/0039-6028(84)90700-3.

[22] M. Fitzsimmons, S. Sass, Quantitative X-ray diffraction study of the atomic structure of the $\sum$=5(Θ = 36.9°) [001] twist boundary in gold, Acta Metall. 36 (1988) 3103–3122, doi:http://dx.doi.org/10.1016/0001-6160(88)90047-8.

[23] P.M. Derlet, S. Van Petegem, H. Van Swygenhoven, Calculation of X-ray spectra for nanocrystalline materials, Phys. Rev. B 71 (2005) 024114, doi:http://dx.doi.org/10.1103/PhysRevB.71.024114.

[24] J. Markmann, V. Yamakov, J. Weissmüller, Validating grain size analysis from X-ray line broadening: a virtual experiment, Scr. Mater. 59 (2008) 15–18, doi:http://dx.doi.org/10.1016/j.scriptamat.2008.02.056.

[25] A. Stukowski, J. Markmann, J. Weissmüller, K. Albe, Atomistic origin of microstrain broadening in diffraction data of nanocrystalline solids, Acta Mater. 57 (2009) 1648–1654, doi:http://dx.doi.org/10.1016/j.actamat.2008.12.011.

[26] G. Kimminau, B. Nagler, A. Higginbotham, W.J. Murphy, N. Park, J. Hawreliak, K. Kadau, T.C. Germann, E.M. Bringa, D.H. Kalantar, H.E. Lorenzana, B.A. Remington, J.S. Wark, Simulating picosecond X-ray diffraction from shocked crystals using post-processing molecular dynamics calculations, J. Phys.: Condens. Matter 20 (2008) 505203, doi:http://dx.doi.org/10.1088/0953-8984/20/50/505203.

[27] M.J. Gutmann, Accelerated computation of diffuse scattering patterns and application to magnetic neutron scattering, J. Appl. Crystallogr. 43 (2) (2010) 250–255, doi:http://dx.doi.org/10.1107/S0021889810002438.

[28] V. Favre-Nicolin, J. Coraux, M.I. Richard, H. Renevier, IUCr, fast computation of scattering maps of nanostructures using graphical processing units, J. Appl. Crystallogr. 44 (3) (2011) 635–640, doi:http://dx.doi.org/10.1107/S0021889811009009.

[29] S.P. Coleman, D.E. Spearot, Atomistic simulation and virtual diffraction characterization of homophase and heterophase alumina interfaces, Acta Mater. 82 (2015) 403–413, doi:http://dx.doi.org/10.1016/j.actamat.2014.09.019.

[30] S.P. Coleman, M.A. Tschopp, C.R. Weinberger, D.E. Spearot, Bridging atomistic simulations and experiments via virtual diffraction: understanding homophase grain boundary and heterophase interface structures, J. Mater. Sci. 51 (2016) 1251–1260, doi:http://dx.doi.org/10.1007/s10853-015-9087-9.

[31] B.D. Butler, T.R. Welberry, Calculation of diffuse scattering from simulated disordered crystals: A comparison with optical transforms, J. Appl. Crystallogr. 25 (1992) 391–399, doi:http://dx.doi.org/10.1107/S0021889891014322.

[32] J. Kacher, C. Landon, B.L. Adams, D. Fullwood, Bragg's Law diffraction simulations for electron backscatter diffraction analysis, Ultramicroscopy 109 (2009) 1148–1156, doi:http://dx.doi.org/10.1016/j.ultramic.2009.04.007.

[33] J. Kacher, J. Basinger, B.L. Adams, D.T. Fullwood, Reply to comment by Maurice et al. in response to "Bragg's Law Diffraction Simulations for Electron Backscatter Diffraction Analysis, Ultramicroscopy 110 (2010) 760–762, doi:http://dx.doi.org/10.1016/j.ultramic.2010.02.004.

[34] S. Villert, C. Maurice, C. Wyon, R. Fortunier, Accuracy assessment of elastic strain measurement by EBSD, J. Microsc. 233 (2009) 290–301, doi:http://dx.doi.org/10.1111/j.1365-2818.2009.03120.x.

[35] C. Maurice, R. Fortunier, J. Driver, A. Day, K. Mingard, G. Meaden, Comments on the paper "Bragg's law diffraction simulations for electron backscatter diffraction analysis" by Josh Kacher, Colin Landon, Brent L. Adams & David Fullwood, Ultramicroscopy 110 (2010) 761–762, doi:http://dx.doi.org/10.1016/j.ultramic.2010.02.003.

[36] T. Britton, C. Maurice, R. Fortunier, J. Driver, A. Day, G. Meaden, D. Dingley, K. Mingard, A. Wilkinson, Factors affecting the accuracy of high resolution electron backscatter diffraction when using simulated patterns, Ultramicroscopy 110 (2010) 1443–1453, doi:http://dx.doi.org/10.1016/j.ultramic.2010.08.001.

[37] A. Winkelmann, C. Trager-Cowan, F. Sweeney, A.P. Day, P. Parbrook, Many-beam dynamical simulation of electron backscatter diffraction patterns, Ultramicroscopy 107 (2007) 414–421, doi:http://dx.doi.org/10.1016/j.ultramic.2006.10.006.

[38] A. Winkelmann, Dynamical effects of anisotropic inelastic scattering in electron backscatter diffraction, Ultramicroscopy 108 (2008) 1546–1550, doi:http://dx.doi.org/10.1016/j.ultramic.2008.05.002.

[39] P.G. Callahan, M. De Graef, Dynamical electron backscatter diffraction patterns. Part I: Pattern simulations, Microsc. Microanal. 19 (2013) 1255–1265, doi:http://dx.doi.org/10.1017/S1431927613001840.

[40] B.E. Jackson, J.J. Christensen, S. Singh, M. De Graef, D.T. Fullwood, E.R. Homer, R.H. Wagoner, Performance of dynamically simulated reference patterns for cross-correlation electron backscatter diffraction, Microsc, Micronanal 22 (2016) 789–802, doi:http://dx.doi.org/10.1017/S143192761601148X.

[41] S. Singh, M. De Graef, Orientation sampling for dictionary-based diffraction pattern indexing methods, Model. Simul. Mater. Sci. Eng. 24 (2016) 085013, doi:http://dx.doi.org/10.1088/0965-0393/24/8/085013.

[42] D. Fullwood, M. Vaudin, C. Daniels, T. Ruggles, S. Wright, Validation of kinematically simulated pattern HR-EBSD for measuring absolute strains and lattice tetragonality, Mater. Charact. 107 (2015) 270–277, doi:http://dx.doi.org/10.1016/j.matchar.2015.07.017.